Automatica 48 (2012) 1751–1758

Contents lists available at SciVerse ScienceDirect

Automatica

journal homepage: www.elsevier.com/locate/automatica

Brief paper

Accounting for hysteresis in repetitive control design: Nanopositioning example☆

Yingfeng Shan, Kam K. Leang [1]

Mechanical Engineering Department, University of Nevada-Reno, Reno, NV 89557-0312, USA

ARTICLE INFO

Article history:
Received 16 March 2011
Received in revised form
10 October 2011
Accepted 19 January 2012
Available online 23 June 2012

Keywords:
Repetitive control
Hysteresis compensation
Nanopositioning
Prandtl–Ishlinskii hysteresis model

ABSTRACT

This paper deals with designing a repetitive controller (RC) for tracking periodic reference trajectories for systems that exhibit hysteresis, such as piezoelectric actuators used in nanopositioning systems. Hysteresis can drastically limit the performance of an RC designed around a linear dynamics model, and thus the effect of hysteresis on the closed-loop stability of RC is analyzed and the allowable size of the hysteresis nonlinearity for a stable RC is quantified. But when the hysteresis effect exceeds the maximum bound, an inverse-hysteresis feedforward controller based on the Prandtl–Ishlinskii hysteresis model is used to compensate for the nonlinearity. The control method is implemented on a custom-designed nanopositioning stage. Experimental results show that by incorporating hysteresis compensation the stability margin and the rate of error reduction improve. Likewise, the maximum tracking error reduces by 71%, from 13.7% (using industry-standard integral control) to 3.9% (using RC with hysteresis compensation), underscoring the benefits of RC with hysteresis compensation.

1. Introduction

Piezoelectric, magnetostrictive, and other types of active (or smart) material actuators employed for motion control and manipulation (*e.g.*, see Clayton, Tien, Leang, Zou, & Devasia, 2009, Tan & Baras, 2004) exhibit hysteresis. The effect alone can lead to over 20% tracking error, for example in piezo-based manipulators (Leang & Devasia, 2007), if left unaccounted for. Furthermore, hysteresis can affect the stability and tracking performance of a closed-loop controller, especially when the controller is designed around a linear model (Main & Garcia, 1997). This work deals with designing a repetitive controller (RC) for tracking periodic reference trajectories for systems that exhibit hysteresis, such as piezoelectric actuators used in nanopositioning systems.

Piezoelectric actuators are commonly used to track a desired motion trajectory that is periodic in time, for example the raster pattern in scanning probe microscopy (Clayton et al., 2009). Such periodic motion is ideally suited for repetitive control, a feedback-based approach that is effective for precision tracking of periodic reference trajectories and/or for rejecting periodic disturbances (Inoue, Nakano, & Iwai, 1981). The RC approach has been applied to a number of applications (Aridogan, Shan, & Leang, 2009; Chew & Tomizuka, 1990; Steinbuch, Weiland, & Singh, 2007). However, the design of RC for hysteretic systems is challenging because the hysteresis effect can drastically affect the performance of the closed-loop system, especially when the RC is designed around a linear dynamics model.

Although the design of RC for nonlinear systems has been studied in the past, *e.g.*, see (Hikita, Yamashita, & Kubota, 1993), the work on quantifying the effect of hysteresis on the stability of an RC system is limited. Typically, the nonlinearity is handled through an internal feedback loop, such as PID (Choi, Lim, & Choi, 2002), to linearize the system dynamics. Feedforward control using an inverse hysteresis model is considered by Ahn (2003). Herein, the input–output behavior of the system is modeled by a static input nonlinearity with an output that drives the linear dynamics (Leang, Zou, & Devasia, 2009). The hysteresis effect is modeled by the Prandtl–Ishlinskii (P–I) approach (Brokate & Sprekels, 1996). The P–I model is a rate-independent phenomenological model and chosen over other models such as the polynomial model, the BoucWen model, the Duhem model, the Maxwell slip model, and the Preisach model (Adriaens, deKoning, & Banning, 2000; Song & Armen, 2006) because of its smaller parameter space and ability for online implementation. Using the P–I model, the effect of hysteresis on the stability of the RC closed-loop system is analyzed to determine the tolerable *size* of the hysteresis nonlinearity for a stable RC system. If, on the other hand, the hysteresis behavior is unacceptably large, a feedforward controller based on the structure of the P–I model is used to compensate for the hysteresis behavior. The control approach is applied to a custom-designed piezo-based nanopositioning stage and experimental tracking results are presented to validate the inverse model and RC design.

☆ The material in this paper was partially presented at the American Control Conference (ACC 2009), June 10–12, 2009, St. Louis, Missouri, USA and the ASME 2011 Conference on Smart Materials, Adaptive Structures and Intelligent Systems (SMASIS), September 18–21, 2011, Scottsdale, Arizona, USA. This paper was recommended for publication in revised form by Associate Editor Pedro Albertos under the direction of Editor Toshiharu Sugie.

E-mail addresses: yingfengshan@gmail.com (Y. Shan), kam@unr.edu (K.K. Leang).

[1] Tel.: +1 775 784 7782; fax: +1 775 784 1701.

0005-1098/$ – see front matter © 2012 Elsevier Ltd. All rights reserved.
doi:10.1016/j.automatica.2012.05.055

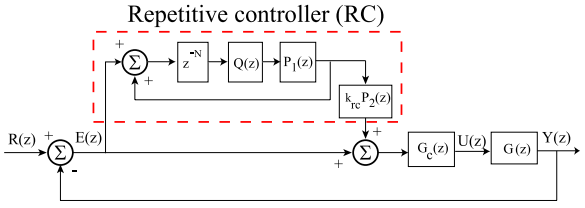

Fig. 1. A plug-in repetitive controller for a linear system.

2. Repetitive control for hysteretic systems

2.1. A plug-in RC for linear systems

A typical plug-in style RC for a linear discrete-time dynamical system $G(z)$ is shown in Fig. 1, where $R(z)$ is a periodic reference trajectory with period T_p. The RC is created by including a pure delay, z^{-N}, inside of a positive-feedback loop to create a signal generator with period T_p, where T_s is the sampling period and $N = T_p/T_s \in \mathbb{N}$ is the number of points per period of the reference trajectory. The low pass filter $Q(z)$ is included to lower the high gain of the RC at high frequencies to ensure stability and robustness (Chew & Tomizuka, 1990). The RC gain, k_{rc}, and the two positive phase-lead compensators, $P_{1,2}(z) = z^{m_{1,2}}$, where m_1, m_2 are non-negative integers, are added to improve tracking performance (Aridogan et al., 2009). Notably, $P_1(z)$ compensates for the phase lag of the low-pass filter $Q(z)$ while $P_2(z)$ compensates for the phase lag of the closed-loop system. Both phase-lead compensators contribute a phase angle of $\theta_i(\omega) = m_i T_s \omega$, for $i = 1, 2$. A typical feedback controller, such as a PID, is represented by $G_c(z)$. Then with $z = e^{j\omega T_s}$ for $\omega \epsilon (0, \pi/T_s)$, the complimentary sensitivity function of the feedback system without the RC is

$$T(e^{j\omega T_s}) = \frac{G_c(e^{j\omega T_s})G(e^{j\omega T_s})}{[1 + G_c(e^{j\omega T_s})G(e^{j\omega T_s})]} = A(\omega)e^{j\theta_T(\omega)}, \tag{1}$$

where $A(\omega) > 0$. Applying the Small-Gain Theorem, the RC system is stable provided that (Aridogan et al., 2009)

$$0 < k_{rc} < \frac{2\cos[\theta_T(\omega) + \theta_2(\omega)]}{A(\omega)}, \tag{2}$$

$$-\pi/2 < [\theta_T(\omega) + \theta_2(\omega)] < \pi/2. \tag{3}$$

2.2. The Prandtl–Ishlinskii hysteresis model

The cascade model structure for the plant shown in Fig. 2(a) is assumed, and the Prandtl–Ishlinskii model is used to represent the hysteresis behavior $\mathcal{H}[\cdot]$. The linear dynamics, such as the structural vibration and creep effect in a piezoactuator (Clayton et al., 2009), are modeled by $G(z)$.

The Prandtl–Ishlinskii model is a phenomenological operator-type model that has recently been used to model the hysteresis in piezoactuators (Janaideh, Su, & Rakheja, 2008). In this model, the output is a weighted sum of play or stop operators (Brokate & Sprekels, 1996). Let the input function $u(t) \in \mathcal{C}_m[t_a, t_b]$, where $\mathcal{C}_m[t_a, t_b]$ represents the space of piecewise continuous monotone functions defined over the interval $\{t : t_a \le t \le t_b; a, b \in \mathbb{N}\}$. The play operator is defined as $\mathcal{P}_r[u](0) = p_r(f(0), 0) = 0$, $\mathcal{P}_r[u](t) = p_r(f(t), \mathcal{P}_r[f](t))$, and $p_r(f(t_i), \mathcal{P}_r[f](t_i)) = \max(f(t_i) - \gamma, \min(f(t_i) + \gamma, \mathcal{P}_r[f](t_{i-1})))$, where $f(t) = g_0 u(t) + g_1$ is a linear function of the control input $u(t)$, g_0 and g_1 are constants, $\gamma = \rho j$, with ρ being a constant, and j is the number of operators. The output $v(t)$ is defined as a weighted sum of play operators, *i.e.*,

$$v(t) = \mathcal{H}[u](t) \triangleq f(t) + \int_0^R d(\gamma)\mathcal{P}_r[u](t)d\gamma, \tag{4}$$

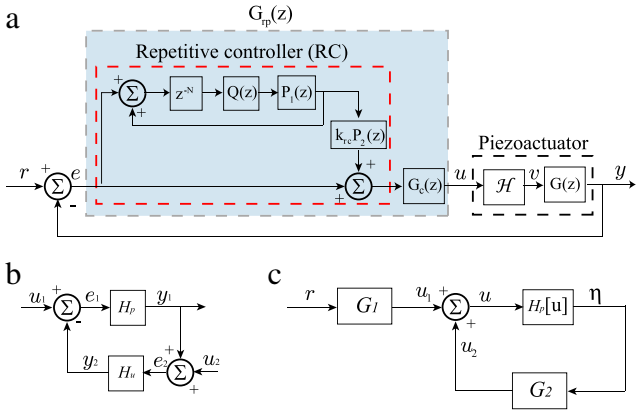

Fig. 2. (a) The nonlinear RC system, where $G_{rp}(z)$ represents the RC and PID controllers. (b) The feedback connection for stability analysis and application of the Small-Gain theorem. (c) An equivalent feedback connection of (a) for analysis.

where $d(\gamma)$ is the density function that controls the shape and size of the output hysteresis curve. The discrete-time version of the hysteresis model (4) can be expressed as

$$v(k) = \mathcal{H}[u](k) \triangleq f(k) + \sum_{j=1}^{n} d(\gamma)\mathcal{P}_r[u](k), \tag{5}$$

where $f(k) = g_0 u(k) + g_1$, k is the time step, and n denotes the number of play operators.

2.3. Stability of RC with hysteresis effect

Consider the linear discrete-time SISO dynamic system $G(z)$ with the following controllable canonical form

$$\begin{aligned} \mathbf{x}(k+1) &= \mathbf{A}\mathbf{x}(k) + \mathbf{B}v(k), \\ y(k) &= \mathbf{C}\mathbf{x}(k) + Dv(k), \end{aligned} \tag{6}$$

where $\mathbf{x} = [x_1, x_2, \ldots, x_n]^T \in \mathbb{R}^n$ is the state vector, $v, y \in \mathbb{R}$ are the input and output, respectively, and $\mathbf{A}$, $\mathbf{B}$, $\mathbf{C}$, D are of compatible dimensions. The RC controller and the controller $G_c(z)$ shown in Fig. 2(a) are lumped into $G_{rp}(z)$ and assumed to have the following discrete-time state–space representation:

$$\begin{aligned} \mathbf{z}(k+1) &= \mathbf{A}_{rp}\mathbf{z}(k) + \mathbf{B}_{rp}e(k), \\ u(k) &= \mathbf{C}_{rp}\mathbf{z}(k) + D_{rp}e(k), \end{aligned} \tag{7}$$

where $\mathbf{z} = [z_1, z_2, \ldots, z_p]^T \in \mathbb{R}^p$ is the controller state vector, $e = r - y \in \mathbb{R}$ is the tracking error, $u \in \mathbb{R}$ is the controller output, and $\mathbf{A}_{rp}$, $\mathbf{B}_{rp}$, $\mathbf{C}_{rp}$, and D_{rp} are of compatible dimensions.

For analysis, the system in Fig. 2(a) is converted to an equivalent feedback connection depicted in Fig. 2(b). To do this, the perturbed system H_p is defined as

$$\eta(k) = H_p[u](k) \triangleq v(k) - g_0 u(k), \tag{8}$$

where $v(k)$ is the output of the discrete-time P–I model (5), and $u(k)$ is the output of the controller (7). The unperturbed system H_u is defined as follows. First, solving for $v(k)$ in Eq. (8) and substituting the expression into Eq. (6), the following system is obtained

$$\begin{aligned} \mathbf{x}(k+1) &= \mathbf{A}\mathbf{x}(k) + \mathbf{B}[\eta(k) + g_0 u(k)], \\ y(k) &= \mathbf{C}\mathbf{x}(k) + D[\eta(k) + g_0 u(k)]. \end{aligned} \tag{9}$$

Recalling the expression for $u(k)$, Eq. (7), $e(k) = r(k) - y(k)$, and D, D_{rp} are finite scalars, the output $y(k)$ can be written as

$$\begin{aligned} y(k) &= \mathbf{C}\mathbf{x}(k) + D[\eta(k) + g_0 u(k)], \\ &= \frac{1}{1 + g_0 D D_{rp}} [g_0 D \mathbf{C}_{rp} \mathbf{C}] \begin{bmatrix} \mathbf{z}(k) \\ \mathbf{x}(k) \end{bmatrix} \\ &\quad + \frac{D}{1 + g_0 D D_{rp}} [\eta(k) + g_0 D_{rp} r(k)]. \end{aligned} \tag{10}$$

Then, using Eqs. (7) and (10), the system's closed-loop dynamics excluding hysteresis can be represented as the unperturbed system H_u, *i.e.*,

$$\begin{bmatrix} \mathbf{z}(k+1) \\ \mathbf{x}(k+1) \end{bmatrix} = \mathbf{A}_L \begin{bmatrix} \mathbf{z}(k) \\ \mathbf{x}(k) \end{bmatrix} + \mathbf{B}_1 r(k) + \mathbf{B}_2 \eta(k),$$

$$u(k) = \mathbf{C}_L \begin{bmatrix} \mathbf{z}(k) \\ \mathbf{x}(k) \end{bmatrix} + D_1 r(k) + D_2 \eta(k), \tag{11}$$

where $\mathbf{A}_L = \begin{bmatrix} \mathbf{A}_{rp} - \frac{g_0 \mathbf{B}_{rp} D \mathbf{C}_{rp}}{1 + g_0 D D_{rp}} & -\frac{\mathbf{B}_{rp} \mathbf{C}}{1 + g_0 D D_{rp}} \\ \frac{g_0 \mathbf{B} \mathbf{C}_{rp}}{1 + g_0 D D_{rp}} & \mathbf{A} - \frac{g_0 \mathbf{B} D_{rp} \mathbf{C}}{1 + g_0 D D_{rp}} \end{bmatrix}$;

$$\mathbf{B}_1 = \begin{bmatrix} \frac{\mathbf{B}_{rp}}{1 + g_0 D D_{rp}} \\ \frac{g_0 \mathbf{B} D_{rp}}{1 + g_0 D D_{rp}} \end{bmatrix}; \qquad \mathbf{B}_2 = \begin{bmatrix} \frac{-\mathbf{B}_{rp} D}{1 + g_0 D D_{rp}} \\ \frac{\mathbf{B}}{1 + g_0 D D_{rp}} \end{bmatrix};$$

$$\mathbf{C}_L = \begin{bmatrix} \frac{\mathbf{C}_{rp}}{1 + g_0 D D_{rp}} & -\frac{D_{rp} \mathbf{C}}{1 + g_0 D D_{rp}} \end{bmatrix};$$

$$D_1 = \frac{D_{rp}}{1 + g_0 D D_{rp}}; \qquad D_2 = \frac{-D D_{rp}}{1 + g_0 D D_{rp}}.$$

The transfer relation for the unperturbed dynamics H_u from inputs $r(k)$ and $\eta(k)$ to output $u(k)$ can be represented in the following input–output form:

$$\begin{aligned} U(z) &= [\mathbf{C}_L (zI - \mathbf{A}_L)^{-1} \mathbf{B}_1 + D_1] R(z) \\ &\quad + [\mathbf{C}_L (zI - \mathbf{A}_L)^{-1} \mathbf{B}_2 + D_2] \eta(z), \\ &= G_1(z) R(z) + G_2(z) \eta(z). \end{aligned} \tag{12}$$

Therefore, the nonlinear RC system in Fig. 2(a) is converted to the equivalent structure shown in Fig. 2(c), which is associated with Eq. (8) (perturbed system H_p) and Eq. (12) (unperturbed system H_u).

Next, it is assumed that the RC closed-loop linear system in Fig. 1 is designed internally stable. By inspection when $g_0 = 1$, then $G_1(z) = G_L(z)$, where $G_L(z) = \frac{U(z)}{R(z)} = \mathbf{C}_L (zI - \mathbf{A}_L)^{-1} \mathbf{B}_1 + D_1$. Therefore with the closed-loop linear system in Fig. 1 designed stable, $G_1(z)$ is BIBO stable, that is, $g_0 \leq M_{G_L}$, where M_{G_L} represents the gain margin of the RC system in Fig. 1. Then what is left to show is the nonlinear system in Fig. 2(a) is stable if the finite gains of $G_2(z)$ and $H_p[u](k)$ satisfy the Small-Gain Theorem (Khalil, 2002).

Let $\|h\|_2$ represent the $\mathcal{L}_2$-norm of a discrete-time function $h(k)$, *i.e.*, $\|h\|_2 = \left(\sum_{k=0}^{\infty} |h(k)|^2\right)^{1/2}$. The finite $\mathcal{L}_2$-gain of $G_2(z)$ in Fig. 2(c) is determined using Parseval's theorem (Khalil, 2002). For example,

$$\begin{aligned} \|u_2\|_2^2 &= \sum_{k=0}^{\infty} u_2^T(k) u_2(k) = \frac{1}{2\pi j} \oint_C z^{-1} U_2(-z) U_2(z) dz, \\ &= \frac{1}{2\pi j} \oint_C z^{-1} \eta(-z) G_2^T(-z) G_2(z) \eta(z) dz \\ &\leq \left(\sup_{\omega \in \mathbb{S}} \|G_2(z)\|_2 \right)^2 \frac{1}{2\pi j} \oint_C z^{-1} \eta(-z) \eta(z) dz \\ &\leq \left(\sup_{\omega \in \mathbb{S}} \|G_2(z)\|_2 \right)^2 \|\eta\|_2^2, \end{aligned} \tag{13}$$

where $z = e^{j\omega T_s}$, $\mathbb{S} \subset (0, \pi/T_s)$ and C is a contour. Thus, the $\mathcal{L}_2$-gain of $G_2(z)$ is

$$\lambda_1 \leq \sup_{\omega \in \mathbb{S}} \|G_2(z)\|_2. \tag{14}$$

In other words, the unperturbed system H_u given by Eq. (12) is finite-gain $\mathcal{L}_2$ stable provided that the $\sup_{\omega \in \mathbb{S}} \|G_2(z)\|_2 < \infty$ and

$$g_0 \leq M_{G_L}. \tag{15}$$

The finite $\mathcal{L}_2$-gain for the perturbed system H_p is determined as follows. First, Eq. (8) is rewritten as

$$\eta(k) = f(k) + \sum_{j=1}^{n} d(\gamma) \mathcal{P}_r[u](k) - g_0 u(k), \tag{16}$$

where $u(k)$ is a piecewise continuous function in k. It is pointed out that the P–I hysteresis model $\mathcal{H}[u]$ is continuous in u (Brokate & Sprekels, 1996; Janaideh, Rakheja, & Su, 2009); therefore, the perturbed system $H_p[u](k)$ is piecewise continuous in k and continuous in $u(k)$. Next, the output of the perturbed system $\eta(k)$ is shown to be bounded in the following form: $\|\eta_\tau\|_2 \leq \lambda_2 \|u_\tau\|_2 + \alpha, \forall \tau \in [0, \infty)$, where α is a nonnegative constant (Khalil, 2002).

Recalling the play operator in the following form

$$\begin{aligned} \mathcal{P}_r[u](k) &= \max(f(k_i) - \gamma, \min(f(k_i) + \gamma, \mathcal{P}_r[f](k_{i-1}))), \\ &\quad \forall i \geq 1, \end{aligned} \tag{17}$$

and noting the range property of the play operator in Brokate and Sprekels (1996), Janaideh et al. (2009), the play operator equation (17) is bounded above and below via $f(k) - \gamma \leq \mathcal{P}_r[u](k) \leq f(k) + \gamma$; hence $|\mathcal{P}_r[u](k)| \leq |f(k)| + |\gamma|$ and

$$\begin{aligned} \left| \sum_{j=1}^{n} d(\gamma) \mathcal{P}_r[u](k) \right| &\leq \sum_{j=1}^{n} |d(\gamma)| \, |\mathcal{P}_r[u](k)| \\ &\leq \sum_{j=1}^{n} |d(\gamma)| \, |f(k)| + \sum_{j=1}^{n} |d(\gamma)\gamma|. \end{aligned} \tag{18}$$

With $f(k) = g_0 u(k) + g_1$,

$$\begin{aligned} \left| \sum_{j=1}^{n} d(\gamma) \mathcal{P}_r[u](k) \right| &\leq \sum_{j=1}^{n} |d(\gamma)| \, |f(k)| + \sum_{j=1}^{n} |d(\gamma)\gamma| \\ &\leq \sum_{j=1}^{n} |d(\gamma)| \, |g_0 u(k)| \\ &\quad + \sum_{j=1}^{n} |d(\gamma)| (|g_1| + |\gamma|). \end{aligned}$$

Then, by the Minkowski inequality (Korn & Korn, 2000), Eq. (16) is bounded as follows:

$$\begin{aligned} \|\eta(k)\|_2 &\leq \left\| \sum_{j=1}^{n} d(\gamma) g_0 u(k) \right\|_2 \\ &\quad + \left\| \sum_{j=1}^{n} |d(\gamma)| (|g_1| + |r|) + g_1 \right\|_2 \\ &\leq \left(|g_0| \sup_{1 \leq j \leq n} \|d(\gamma)\|_1 \right) \|u(k)\|_2 + \alpha, \end{aligned} \tag{19}$$

where $\alpha = \left\| \sum_{j=1}^{n} |d(\gamma)| (|g_1| + |r|) + g_1 \right\|_2$ is a nonnegative constant. Therefore, the finite gain for the perturbed system H_p such that it is $\mathcal{L}_2$ stable is

$$\lambda_2 \leq |g_0| \sup_{1 \leq j \leq n} \|d(\gamma)\|_1, \tag{20}$$

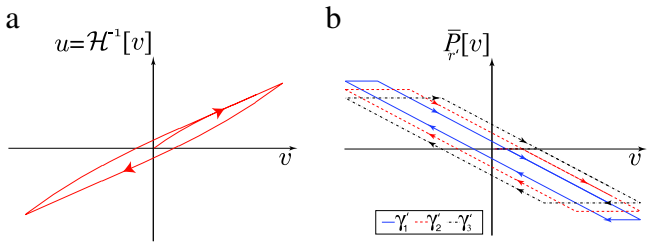

Fig. 3. (a) Input versus measured output plot. (b) A play-type operator for the inverse model with threshold γ_i'.

where $\|\cdot\|_1$ is the $\mathcal{L}_1$ norm. The finite gain λ_2 is proportional to the size of the P–I model's density function.

Finally, according to the Small-Gain Theorem, the nonlinear RC system is finite-gain $\mathcal{L}_2$ stable if $\lambda_1\lambda_2 < 1$; therefore, the nonlinear closed-loop RC system is input–output stable provided that $g_0 \leq M_{G_L}$ [Eq. (15)] and

$$\sup_{1\leq j\leq n} \|d(\gamma)\|_1 < \frac{1}{|g_0| \sup_{\omega\in\mathbb{S}} \|G_2(z)\|_2}. \tag{21}$$

As long as the conditions given by Eqs. (15) and (21) are satisfied, the RC system is stable. In addition, Eq. (21) quantifies the tolerable *size* of the hysteresis nonlinearity for a stable RC.

3. P–I feedforward hysteresis compensation

For a system where the hysteresis is unacceptably large, a feedforward controller is used to compensate for the hysteresis effect. The hysteresis compensator takes the same structure as the forward P–I model. The characteristics of the inverse model is based on the shape of the inverse hysteresis curve, that is, the input versus output curve shown in Fig. 3(a) (u versus v plot). It is noted that as the output v increases, the input u increases but traverses onto an upper branch of the inverse–hysteresis curve. Therefore, a candidate play-type operator for the inverse–hysteresis model is shown in Fig. 3(b) and is defined as

$$\begin{aligned}\overline{P}_{r'}[v](0) &= \overline{p}_{r'}(h(0), 0) = 0,\\ \overline{P}_{r'}[v](t) &= \overline{p}_{r'}(h(t), \overline{P}_{r'}[h](t)),\end{aligned} \tag{22}$$

where $\overline{p}_{r'}(h(t_i), \overline{P}_{r'}[h](t_i)) = \max(-h(t_i) - \gamma', \min(-h(t_i) + \gamma', \overline{P}_{r'}[h](t_{i-1})))$, $h(t) = g_0'v(t) + g_1'$ with constants g_0' and g_1', and $v(t)$ is the output of the hysteresis behavior. The constant γ' denotes the threshold of the inverse play operator. Finally, the output of the inverse hysteresis model is

$$\mathcal{H}^{-1}[v](t) \triangleq h(t) + \int_0^R d_{inv}(\gamma')\overline{P}_{r'}[v](t)d\gamma', \tag{23}$$

where $d_{inv}(\gamma')$ is a density function.

4. The experimental system and modeling

4.1. The experimental nanopositioning system

The control approach is evaluated on the x-axis of a custom-made three-axis serial-kinematic nanopositioner (see Fig. 4), where plate-stack piezoactuators (5 × 5 × 10 mm Noliac SCMAP07) are used to drive the sample platform along the x, y, and z directions. The nanopositioner has a travel range of approximately 10 × 10 × 3 μm. The lateral displacement of the platform is measured by inductive sensors (Kaman SMU9000-15N). Due to the low mass of the sample platform nested within,

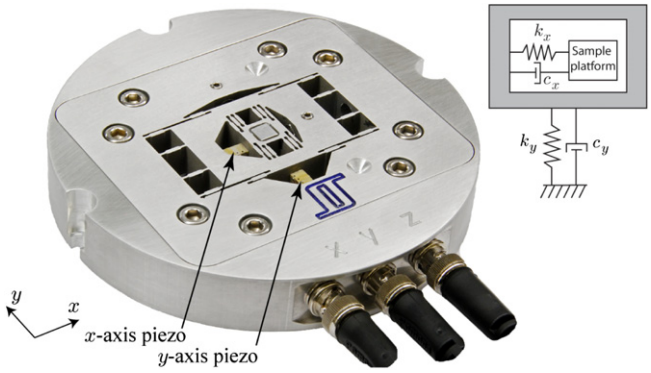

Fig. 4. Custom-made three-axis serial-kinematic piezo-based nanopositioner.

the dominant resonant frequency on the x-axis is about 18 kHz, and it is just 4.7 kHz for the y-axis because of the larger size and mass of the y-stage. The positioner is created specifically for scanning-type applications, such as the rastering movements in AFM imaging where one lateral axis moves much faster (≥100-times) than the other axis. Therefore, tracking periodic reference trajectories with precision is highly desirable.

The experimental setup includes a custom-made analog PID controller circuit, a field programmable gate array (FPGA) system (National Instruments cRIO-9002 controller with 16-bit plug-in analog input and analog output modules) for implementing the RC and feedforward controllers, a piezo amplifier (gain $A = 20$ V/V), and a desktop computer with data acquisition hardware (NI-PCI-6221, 16-bit resolution, maximum sampling frequency of 250 kHz) for sending and collecting data. The closed-loop bandwidth of the FPGA, maximum of 100 kHz, is limited by the sampling frequency of the input/output modules. The FPGA system is programmed using the NI-LabVIEW FPGA Toolkit, where the software package generates the VHDL code, then the code is downloaded to the FPGA target via an Ethernet cable.

4.2. Dynamics and hysteresis modeling

A linear 9th-order transfer function model $G(s)$ is determined by curve-fitting the measured frequency response of the nanopositioner (x-axis). A discrete-time model $G(z)$ is obtained using the c2d command in Matlab with a sampling frequency of 100 kHz.

The hysteresis model for the x-axis is determined by actuating the piezo at the full-range displacement of 10 μm using a 1 Hz triangle input signal. The measured response (solid line) is shown in Fig. 5(a). Then the command voltage $u(t)$ and the measured displacement response $y(t)$ are imported to a Matlab least-squares optimization program to estimate the parameters of the P–I model. Finally, the hysteresis model parameters are optimized to: $g_0 = 0.8331$, $g_1 = 0.0677$, $\lambda = 0.0211$, $\delta = -5.0194$ and $\rho = 0.1079$ for $d(r) = \lambda e^{-\delta\gamma}$. The performance of the P–I model is compared to the measured output in Fig. 5. The results show that the hysteresis model output matches the measured output well with a maximum error of approximately 2.1%.

Both models (hysteresis and dynamics) are combined to create the cascade model structure and the output of this model is compared to the measured open-loop response of the piezoactuator. The results are shown in Fig. 6 for a ±5 μm displacement range, scanning at 10 Hz, 100 Hz, 1 kHz using a triangle input signal. As can be seen, the maximum modeling error is approximately 2.05% up to 1 kHz (plots (a1) through (c2)). Finally, when the piezoactuator is driven with a 2 kHz sinusoidal input signal, the maximum modeling error is approximately 2.12% (see Fig. 6(d1) and (d2)). Therefore, the cascade model structure is a good representation of the combined effects of hysteresis and dynamics in the piezoactuator.

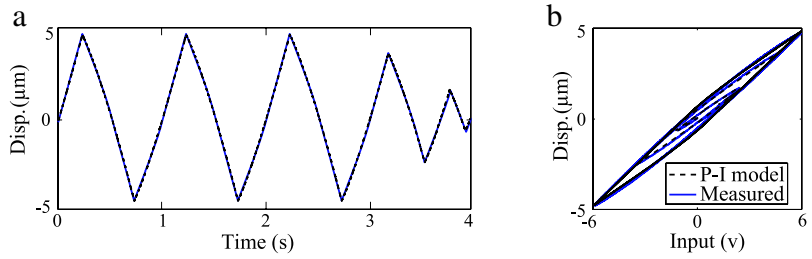

Fig. 5. Comparison between measured hysteresis behavior (solid line) and the output of the P–I hysteresis model (dashed line): (a) time response and (b) the hysteresis curves. The results show good agreement.

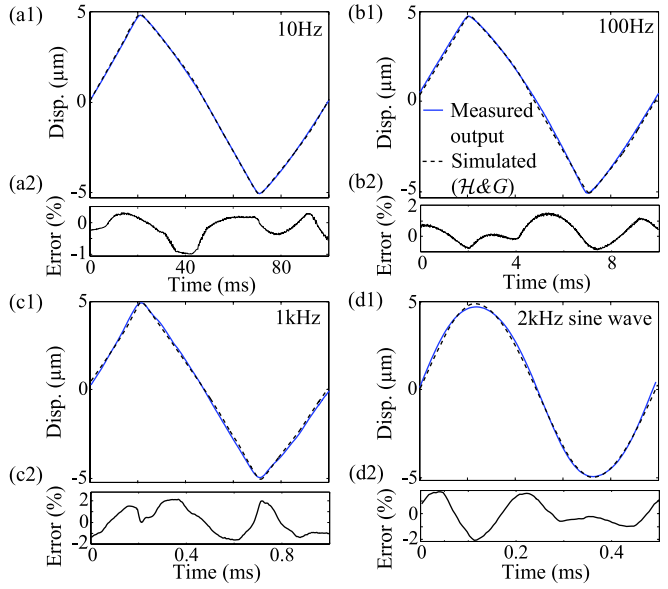

Fig. 6. Experimental validation of the P–I model, $\mathcal{H}[\cdot]$, and the linear dynamics model, $G(z)$. Displacement and error vs. time between measured (solid line) and model output (dashed line): (a1) and (a2) 10 Hz triangle scanning motion; (b1) and (b2) 100 Hz triangle scanning motion; (c1) and (c2) 1 kHz triangle scanning motion; and (d1) and (d2) 2 kHz sinusoidal scanning motion.

4.3. Inverse P–I hysteresis model

The parameters for the inverse P–I hysteresis model, $\mathcal{H}^{-1}$, are obtained from the measured input–output data from the forward model, where the measured output becomes the input to the inverse model, and the input becomes the model output (Fig. 7(a)). For convenience, the density function is chosen as $d_{inv}(\gamma') = \lambda' e^{-\delta'\gamma'}$, where $\gamma' = \rho' j$ is the threshold of the inverse hysteresis operator with $j = 1, 2, \ldots, 8$, and λ', δ', ρ' are real constants. The constants are found using a nonlinear least-square optimization function created in Matlab. The parameters are determined as $g_0' = 1.1354$, $g_1' = -0.3109$, $\lambda' = 0.0211$, $\delta' = -1.813$ and $\rho' = 0.527$. It is pointed out that λ', δ' and ρ' affect the size and the slope of the inverse hysteresis curve.

Fig. 7(b) shows the performance of the $\mathcal{H}^{-1}$ model to compensate for hysteresis, where relatively linear response is achieved. To further validate the inverse model, the $\mathcal{H}^{-1}$ is applied to the piezoactuator to compensate for the hysteresis behavior over different frequencies. By compensating for hysteresis, the output response is dominated by the dynamic effects, $G(z)$, as shown in Fig. 8 for a triangular scanning motion at 10 Hz, 100 Hz, 1 kHz, and a 2 kHz sinusoidal scan motion. As the frequency increases, the resulting loop-like appearance is due to the phase shift between the input and output, and not the hysteresis effect. A comparison is made between the measured response and the simulated response from just the dynamics model, and the results show that the maximum error is approximately 1.17% and 1.3% at 1 kHz and 2 kHz, respectively. The results also show that the hysteresis effect can be compensated for using the proposed inverse model, leaving behind only the dynamics behavior.

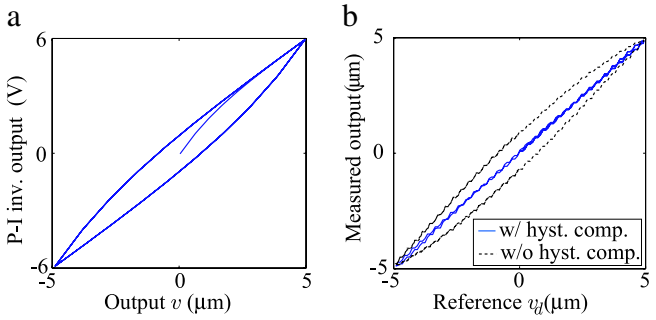

Fig. 7. (a) Inverse hysteresis model. (b) The hysteresis curves for the piezoactuator with (solid line) and without (dashed line) feedforward compensation.

5. Controller design and implementation

In the controller block diagram shown in Fig. 2(a), $G_c(z)$ is chosen as a proportional–integral (PI) controller, where the gains are tuned using the linear dynamics model to $K_p = 1.3$ and $K_i = 40\,000$ (particularly the Ziegler–Nichols method is used to provide the starting point for tuning the gains). Next, the RC is designed based on the dynamics model $G(z)$ and the controller $G_c(z)$. The process includes designing a low-pass filter $Q(z)$ and phase lead compensator z^{m_2} to satisfy the condition in Eq. (3) for stability and robustness; followed by tuning the RC gain k_{rc} and z^{m_1} for good tracking performance. The low-pass filter is $Q(z) = \frac{a}{z+b}$ with $|a| + |b| = 1$. The cutoff frequency is determined by finding the lowest frequency such that $\theta_T(\omega) + \theta_2(\omega)$ is within the $\pm 90^\circ$ (Eq. (3)) bound (Aridogan et al., 2009). The phase response $\theta_T(\omega) + \theta_2(\omega)$ is shown in Fig. 9, and without the phase lead compensator ($m_2 = 0$) the cutoff frequency is approximately 7.3 kHz. By considering that the maximum scanning rate is 1 kHz and the hardware limitation of the FPGA system, the phase lead compensator is selected as $m_2 = 0$ to have a 7 kHz cutoff frequency.

The RC gain is chosen as $k_{rc} = 0.8$ to satisfy Eq. (2). Then the phase lead z^{m_1} is tuned in simulation by looking at the maximum tracking error versus different m_1 values for tracking a 1 kHz triangle trajectory over a range of 10 μm. It is determined that the lowest maximum tracking error is achieved with $m_1 = 6$. Therefore, the parameters for the RC controller are chosen as $m_1 = 6$, $m_2 = 0$, $k_{rc} = 0.8$ and the cutoff frequency for $Q(z)$ is 7 kHz. In the experiments, the RC and $\mathcal{H}^{-1}$ are implemented on the FPGA hardware with a closed-loop sampling frequency of 100 kHz.

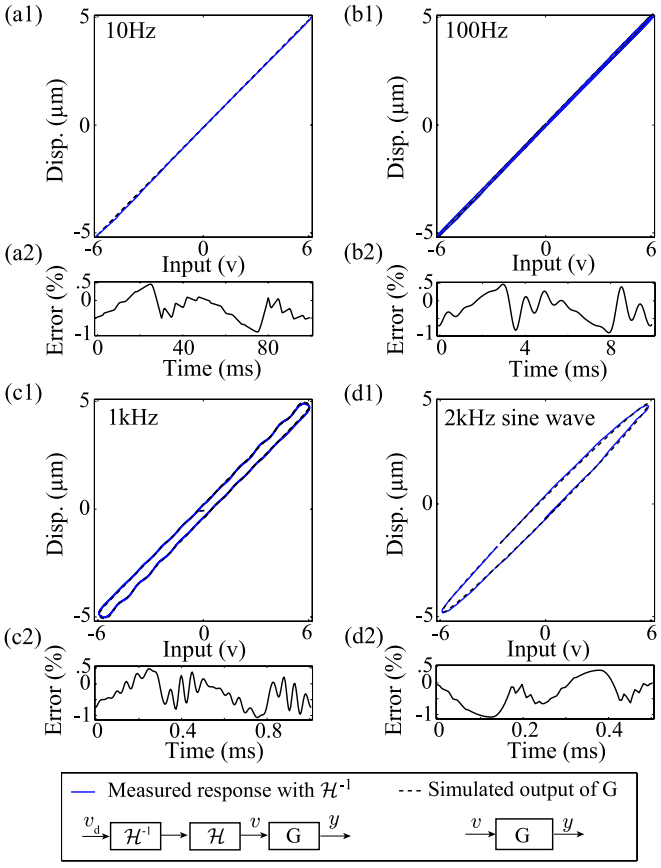

Fig. 8. Validating cascade model by compensating for hysteresis. Comparison of output vs. input plots and error for: (a1) and (a2) 10 Hz triangular trajectory; (b1) and (b2) 100 Hz triangular trajectory; (c1) and (c2) 1 kHz triangular trajectory; and (d1) and (d2) 2 kHz sinusoidal trajectory.

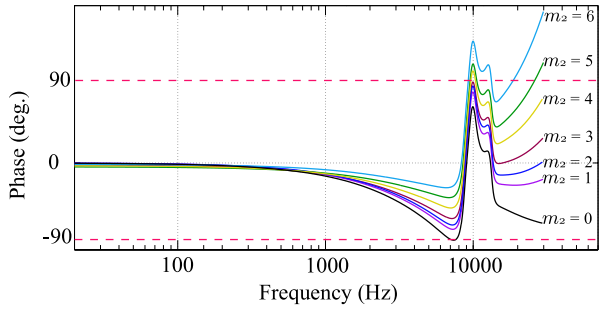

Fig. 9. Phase response $[\theta_T(\omega)+\theta_2(\omega)]$ of the feedback closed-loop system without RC, with phase lead z^{m_2}.

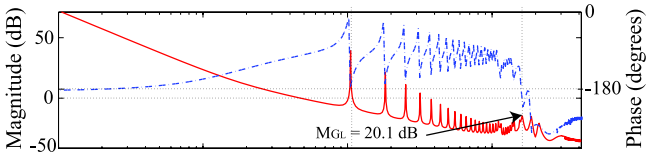

Fig. 10. Frequency response of the open-loop linear RC system showing the gain margin M_{G_L}.

5.1. Quantifying the effect of hysteresis

The effect of hysteresis on RC stability is quantified using the stability conditions given in Eqs. (15) and (21). First, the gain margin of the linear RC system is found from the frequency response of the RC system to be $M_{G_L} = 20.1$ dB (magnitude of 10.12) (Fig. 10). Compared to the constant g_0 from the forward P–I model, $g_0 = 0.8331 < M_{G_L} = 10.12$. Thus, the first part of the stability conditions, Eq. (15), is satisfied.

Now for the second part of the stability condition given by Eq. (21), $G_{rp}(z)$ is written as $G_{rp}(z) = \frac{G_c(z)}{1-z^{-N+m_1}Q(z)}$, where $z^{-N+m_1} = z^{-94}$, $Q(z) = 0.3558/(z-0.6442)$, $k_{rc} = 0.8$, and $G_c = 1.3 + 0.4z/(z-1)$ with sampling frequency $F_s = 100$ kHz. It is then determined that the $\sup_{\omega\in\mathbb{S}} \|G_2(z)\|_2 = 5.31$, which implies that $1/|g_0| \sup_{\omega\in\mathbb{S}} \|G_2(z)\|_2 = 0.222$. Compared to the $\sup_{1\le j\le n} \|d(\gamma)\|_1 = 0.409$, the second part of the stability condition, Eq. (21), is not satisfied. Therefore, direct implementation of the RC can cause the closed-loop system to be unstable, likely requiring hysteresis compensation.

6. Simulation and experimental results

6.1. RC stability

The effect of hysteresis on RC stability is studied in simulation and experiments. The simulation is performed in Matlab using the RC, $G_c(z)$, $G(z)$, and the P–I hysteresis model. The experiment is done using the same controllers, where the proportional–integral controller, $G_c(z)$, is implemented using the analog hardware and the RC is implemented using the FPGA hardware. Finally, the $\mathcal{H}^{-1}$ is investigated in simulation and experiments to further study the effect of hysteresis on system stability.

First, the piezoactuator's hysteresis behavior is modeled by the P–I approach as shown in Fig. 11 (a1), where its size is determined to 0.409 by Eq. (21). Using this model, the simulated response of the RC control system is shown in Fig. 11. It can be readily seen from the simulation that the size of the nonlinearity causes the response to exhibit excessive oscillation, indicating the onset of instability. The experimental results using the same controller

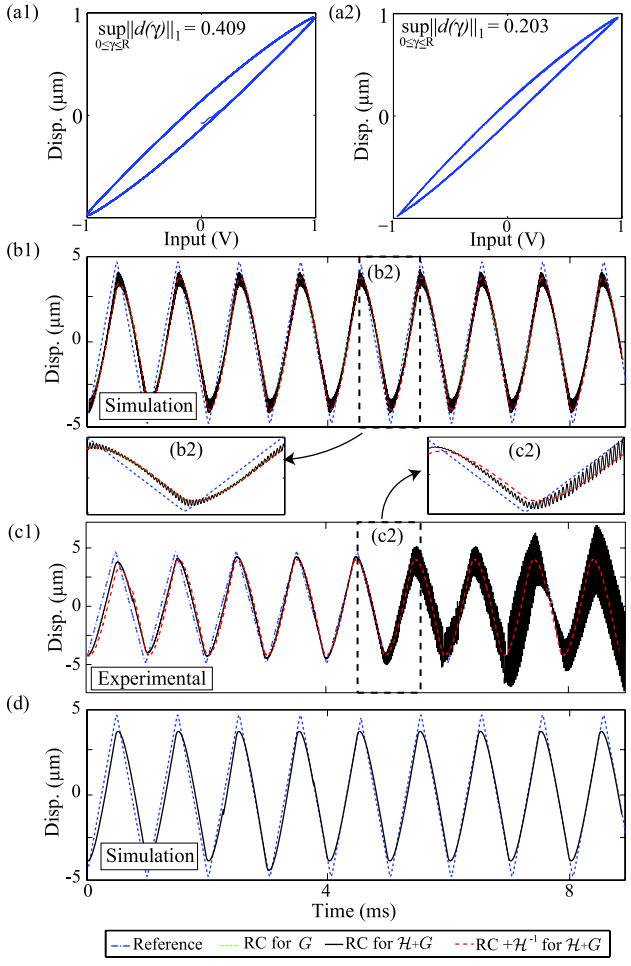

Fig. 11. The effect of hysteresis on RC stability for tracking 1 kHz triangle trajectory: (a1) and (a2) Size of hysteresis nonlinearity. (b1) and (b2) Simulation results using hysteresis in (a1). (c1) and (c2) Experimental results for hysteresis in (a1). (d) Simulation result using hysteresis in (a2).

shows similar behavior as illustrated in Fig. 11. The RC system begins to show signs of becoming unstable at approximately 4.5 ms, indicating that the hysteresis effect, when significant, reduces the stability margin of the closed-loop system. However, the simulated response of the RC controller where the hysteresis nonlinearity is smaller (Fig. 11(a2)) is stable (see Fig. 11(d)).

6.2. Hysteresis compensation for precision tracking

The PI controller gains can be re-designed to stabilize the system, rather than use hysteresis compensation, for example to $k_p = 1.1$ and $k_i = 40\,000$ to satisfy the stability conditions and for good tracking performances. Experiments are done to evaluate the tracking performance for standard proportional–integral control and RC with and without hysteresis compensation. The performance measures of the controllers for tracking triangular reference trajectories at 10 Hz, 100 Hz, and 1 kHz are listed in Table 1, comparing the maximum tracking error [$e_{\max}(\%)$] and root-mean-square error [$e_{\text{rms}}(\%)$]. The tracking error of the 1 kHz example is shown in Fig. 12, where plot (a), (b), and (c) are the tracking error versus time and (d) is the displacement versus time at steady state. It can be seen that the maximum tracking error of the proportional–integral controller combined with the $\mathcal{H}^{-1}$ is reduced from 13.7% to 12.0%. By using just the proportional–integral controller and the RC, the tracking error is reduced to 4.5%. Finally, the addition of $\mathcal{H}^{-1}$ lowers the maximum tracking error to 3.9% (71% reduction). In addition to reducing the tracking errors of proportional–integral controller and the RC, the hysteresis compensator also increases the rate that the tracking error converges, from 4.2 to 3.6 ms, a 14% reduction as shown in Fig. 12(c).

Table 1
Steady-state tracking results (% of total range).

Controller	10 Hz		100 Hz		1 kHz	
	$e_{\max}$	e_{rms}	$e_{\max}$	e_{rms}	$e_{\max}$	e_{rms}
PI	2.37	1.36	5.52	4.04	13.7	11.42
PI + $\mathcal{H}^{-1}$	1.73	1.10	3.99	2.46	12.0	9.46
PI+RC	0.99	0.42	1.77	0.69	4.50	1.60
PI + RC + $\mathcal{H}^{-1}$	0.72	0.28	1.26	0.46	3.90	1.38

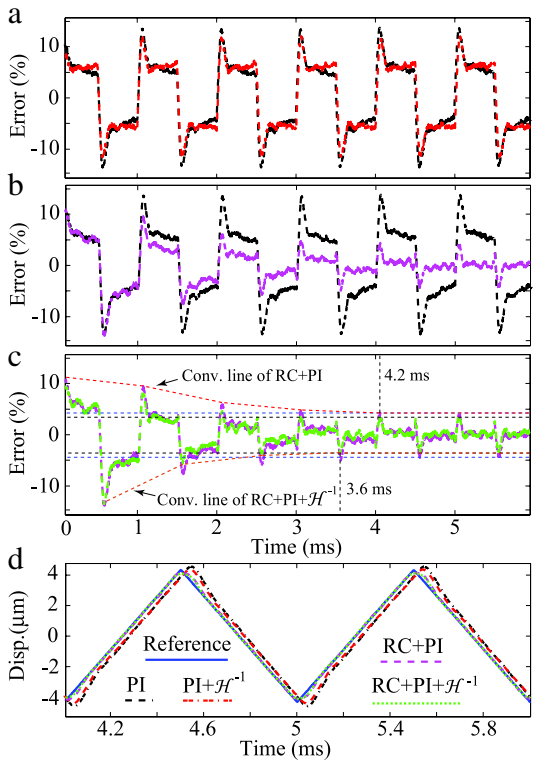

Fig. 12. Tracking results for scanning at 1 kHz: (a) Proportional–integral with and without $\mathcal{H}^{-1}$; (b) PI and RC (without $\mathcal{H}^{-1}$); (c) PI + RC and PI + RC + $\mathcal{H}^{-1}$; and (d) steady-state displacement versus time.

7. Conclusions

This paper focused on analyzing the effect of hysteresis on the stability of RC. The Prandtl–Ishlinskii model was used to characterize the hysteresis behavior and the model parameters were then used to determine the bounds for a stable RC system. The control approach was implemented on a custom-design nanopositioning system, where results showed a significant improvement in tracking performance (such as a 71% reduction in tracking error).

References

Adriaens, H. J. M. T. A., de Koning, W. L., & Banning, R. (2000). Modeling piezoelectric actuators. *IEEE/ASME Transactions on Mechatronics*, *5*(4), 331–341.

Ahn, H.-S. (2003). Design of a repetitive control system for a piezoelectric actuator based on the inverse hysteresis model. In *The fourth international conference on control and automation*. Montreal, Canada (pp. 128–132).

Aridogan, U., Shan, Y., & Leang, K. K. (2009). Design and analysis of discrete-time repetitive control for scanning probe microscopes. *ASME Journal of Dynamic Systems, Measurement, and Control*, *131*, 061103. 12 pages.

Brokate, M., & Sprekels, J. (1996). *Hysteresis and phase transitions*. New York: Springer.

Chew, K. K., & Tomizuka, M. (1990). Digital control of repetitive errors in disk drive systems. *IEEE Control Systems Magazine*, *10*(1), 16–20.
Choi, G. S., Lim, Y. A., & Choi, G. H. (2002). Tracking position control of piezoelectric actuators for periodic reference inputs. *Mechatronics*, *12*(5), 669–684.
Clayton, G. M., Tien, S., Leang, K. K., Zou, Q., & Devasia, S. (2009). A review of feedforward control approaches in nanopositioning for high speed SPM. *ASME Journal of Dynamic Systems, Measurement, and Control*, *131*(6), 061101.
Hikita, H., Yamashita, M., & Kubota, Y. (1993). Repetitive control for a class of nonlinear systems. *JSME International Journal*, *36*(4), 430–434.
Inoue, T., Nakano, M., & Iwai, S. (1981). High accuracy control of a proton synchrotron magnet power supply. In *Proc. 8th world congr. IFAC. Vol. 20* (pp. 216–221).
Janaideh, M. A., Rakheja, S., & Su, C. (2009). A generalized Prandtl–Ishlinskii model for characterizing the hysteresis and saturation nonlinearities of smart actuators. *Smart Materials and Structures*, *18*(4), 045001–045009.
Janaideh, M. A., Su, C.-Y., & Rakheja, S. (2008). Development of the rate-dependent Prandtl–Ishlinskii model for smart actuators. *Smart Materials and Structures*, *17*, 035026. 11pp.
Khalil, H. K. (2002). *Nonlinear systems* (3rd ed.). Prentice-Hall.
Korn, G. A., & Korn, T. M. (2000). *Mathematical handbook for scientists and engineers: definitions, theorems, and formulas for reference and review*. New York: Dover Publications.
Leang, K. K., & Devasia, S. (2007). Feedback-linearized inverse feedforward for creep, hysteresis, and vibration compensation in AFM piezoactuators. *IEEE Transactions on Control Systems Technology*, *15*(5), 927–935.
Leang, K. K., Zou, Q., & Devasia, S. (2009). Feedforward control of piezoactuators in atomic force microscope systems: inversion-based compensation for dynamics and hysteresis. *IEEE Control Systems Magazine*, *29*(1), 70–82.
Main, J. A., & Garcia, E. (1997). Piezoelectric stack actuators and control system design: strategies and pitfalls. *AIAA Journal of Guidance, Control, and Dynamics*, *20*(3), 479–485.
Song, J., & Armen, D. K. (2006). Generalized Bouc–Wen model for highly asymmetric hysteresis. *Journal of Engineering Mechanics*, *132*(6), 610–618.
Steinbuch, M., Weiland, S., & Singh, T. (2007). Design of noise and period-time robust high-order repetitive control, with application to optical storage. *Automatica*, *43*(12), 2086–2095.
Tan, X., & Baras, J. S. (2004). Modeling and control of hysteresis in magnetostrictive actuators. *Automatica*, *40*, 1469–1480.

Yingfeng Shan received his M.S. degree in Mechanical Engineering from Virginia Commonwealth University, Richmond, Virginia, in 2008, and his Ph.D. degree in Mechanical Engineering from the University of Nevada-Reno in 2011. From 2005 to 2006, he was a Control Engineer in China National Petroleum Corp., China. He is currently employed as a Controls Engineer at Electro Scientific Industries, Inc., in Portland, Oregon. His expertise is in micro- and nanoscale motion control systems.

Kam K. Leang received his B.S. and M.S. degrees in Mechanical Engineering from the University of Utah, Salt Lake City, Utah, in 1997 and 1999, respectively, and his Ph.D. degree from the University of Washington, Seattle, Washington, in December 2004. He is an Associate Professor in the Mechanical Engineering Department at the University of Nevada-Reno, Reno, Nevada, where he joined in 2008. From 2005 to 2008, he taught in the Mechanical Engineering Department at Virginia Commonwealth University, Richmond, Virginia. His research interests include modeling and control of piezoactuators for scanning probe microscopy applications, fabrication and control of electroactive polymers, and design of microelectromechanical systems (MEMS) for nanotechnology. He is a member of ASME, IEEE, and SPIE.